

Article

Integrated Geochemical and Morphological Data Provide Insights into the Genesis of Ferromanganese Nodules

Mariana Benites ^{1,*}, Christian Millo ¹, James Hein ², Bejugam Nagender Nath ³,
Bramley Murton ⁴, Douglas Galante ⁵ and Luigi Jovane ¹

¹ Instituto Oceanográfico, Universidade de São Paulo, São Paulo 05508-120, Brazil; millo@usp.br (C.M.); jovane@usp.br (L.J.)

² United States Geological Survey, Santa Cruz, CA 95060, USA; jhein@usgs.gov

³ National Institute of Oceanography, Dona Paula 403004, India; nagendernath@yahoo.com

⁴ National Oceanographic Centre, Southampton SO14 3ZH, UK; bramley.murton@noc.ac.uk

⁵ Brazilian Synchrotron Light Laboratory, Campinas 13083-100, Brazil; douglas.galante@lnls.br

* Correspondence: mariana.benites@usp.br; Tel.: +55-11-3091-6571

Received: 18 September 2018; Accepted: 19 October 2018; Published: 26 October 2018



Abstract: Ferromanganese nodules grow by precipitation of metals from seawater and/or sediment pore water. The formation of different genetic types depends on the composition and redox conditions of the water and upper sediment layers, water depth, and primary productivity in surface waters. Many characteristics of nodules have been used to investigate their genesis. In this paper, we compare nodules from different environments using Computed Tomography, Scanning Electron Microscopy-Energy Dispersive X-ray Spectroscopy, and Micro X-ray Fluorescence data to better understand how geochemical differences are linked to different morphological features. We use representative samples of purely hydrogenetic nodules and mixed-type nodules with various proportions of hydrogenetic and diagenetic growth laminae. Our results show a micrometric alternation between high-absorbance massive Mn-enriched (Mn/Fe up to 40) laminae and low-absorbance dendritic Mn-depleted (Mn/Fe about 1) laminae in mixed-type nodules, suggesting the rhythmic alternation of hydrogenetic oxic conditions and suboxic diagenetic input. This micro-rhythmic alternation is absent in purely hydrogenetic nodules, which are homogenous both chemically and morphologically. A conceptual model is proposed to account for these geochemical and morphological differences in terms of the vertical migration of the oxic-suboxic front relative to the base of the nodules.

Keywords: ferromanganese nodules; growth conditions; diagenesis; CT tomography; μ -XRF

1. Introduction

Marine ferromanganese (hereafter Fe–Mn) nodules are Fe and Mn oxides precipitated concentrically around a nucleus [1–3]. Deep-ocean Fe–Mn nodules are generally found at the sediment-water interface on abyssal plains [1,4,5]. Nodules form in different sedimentary settings, from oxic red clays to suboxic organic carbon-rich sediments [6,7].

Iron and manganese oxides precipitated from oxic seawater are called hydrogenetic, and those from sediment pore water are called diagenetic. Both are accompanied by the sorption of trace and rare earth elements (REE) on the Fe and Mn oxides [5,8–10]. The precipitation occurs concentrically around a nucleus, which is any hard material available in the environment, e.g., rock fragments, pumice, consolidated sediments, pieces of biological material like bone fragments and shark's teeth, and old nodule fragments [11]. The precipitation rate of Fe–Mn oxides is of the order of a few mm per Myr

(million years) for hydrogenetic nodules and because the extent of reactive surface in the nanophase materials is large, they acquire high contents of economically important metals from ocean water and pore waters such as Ni, Cu, Co, Mo, Zr, REE, and Li. Many of these elements, especially those important to future low-carbon societies, are being considered for deep-ocean mining [12–18].

Three classes of Fe–Mn nodules have been recognized: hydrogenetic, diagenetic and mixed-type. Hydrogenetic nodules derive all elements from oceanic bottom waters, whereas diagenetic nodules derive elements from redox cycling during early diagenetic reactions of organic matter in the sediment [19–23]. The transition from diagenetic to hydrogenetic processes depends on the redox conditions in the environment of formation [11,19,24], including the depth of the oxic/suboxic redox front (OSF) in the sediment. Oxidation plays only a minor role in nodule formation, if any. This is a conclusion that is supported by X-ray photoelectron spectroscopy measurements [25]. Mixed-type nodules are composed of various proportions of the diagenetic and hydrogenetic end-member laminae [4,26]

In order to classify nodules according to these three types, some studies have relied on chemical proxies such as Mn/Fe ratio, trace elements, and REE contents [7,8,11,24,27]. Other studies relied on morphological characteristics such as shape, size, surface texture, internal lamination, and nucleus type [4,28–31]. These parameters reflect the sedimentary environment of formation, and provide insight into nodule genesis [1,32,33]

Redox conditions affect nodule chemistry. For example, during anoxic diagenesis in the sediment, Mn-oxide reduction releases Mn, Ni, Cu, and Li into the pore water that then diffuses up into the adjacent suboxic diagenetic zone [34–36]; in contrast, Co is acquired by the nodules solely through sorption from seawater under oxic conditions [23]. Fe occurs predominantly as Fe^{3+} complexed with OH in oxic seawater [33]. The redox potential determines in which oxidation state Fe and Mn will occur in the nodules. Fe^{3+} precipitates predominantly as $\text{FeO}(\text{OH})$ in oxic environments, Mn generally precipitates as Mn^{4+} and Mn^{3+} mixed oxides under oxic conditions, while minor Mn^{2+} may be present in nodules under suboxic conditions [37,38] depending on the location of the oxic-suboxic redox boundary. Environmental conditions may change during nodule formation, therefore impacting their genesis. Geochemical information combined with morphological and internal structural data provide an integrated approach to better understand these processes of nodule formation.

Here, we apply Computed Tomography (CT), Scanning Electron Microscopy–Energy Dispersive X-ray Spectroscopy (SEM-EDS), and Micro X-ray Fluorescence (μXRF) analysis to better understand the genesis of Fe–Mn nodules and how geochemical differences match different morphological features. We use representative samples from well-known Fe–Mn nodule deposits previously described in the literature (Table 1): Typical mixed-type nodules from the Clarion-Clipperton Zone (CCZ) [39,40]; typical mixed-type nodules from the Central Indian Basin (CIB) [7,21], typical oxic hydrogenetic nodules from the Mascarene Basin (MB) [41]; and a hydrogenetic Fe–Mn-coated pebble from the Rio Grande Rise (RGR) (this paper). Our results indicate that an integration of geochemical and morphological features is best suited to genetically characterize Fe–Mn nodules.

Table 1. Provenance, geographic coordinates, genetic type, and main characteristics of nodules analyzed here.

Samples ID	Latitude		Longitude		Depth (m)	Genetic Type	Characteristics	References
Clarion-Clippertone Zone								
JC120-104A	13°	30.700'	−116°	35.166'	4130	Mixed-type	Discoidal shape with rim marking the water-sediment interface.	[39,40]
JC120-104B	13°	30.700'	−116°	35.166'	4130			
JC120-104C	13°	30.700'	−116°	35.166'	4130			
JC120-104D	13°	30.700'	−116°	35.166'	4130			
Central Indian Basin								
AAS40-308	−12°	03.642'	74°	29.844'	5060	Mixed-type	Nodules from the CIB vary from diagenetic to hydrogenetic depending on type of sediments (red clays, carbonate ooze, siliceous ooze, etc.).	[7,21]
AAS21-17	−12°	30.204'	75°	54.936'	5410			
AAS21-19	−12°	25.098'	75°	50.178'	5350			
SS4-280	−12°	00.000'	76°	30.540'	5400			
F8-398A	−15°	29.040'	75°	59.460'	5150			
Mascarene Basin								
SK35-24	−15°	02.400'	55°	04.000'	4420	Hydrogenetic	Spheroidal to sub-spheroidal shape, 2–4 cm in size, smooth surface, Fe-Co-REE-enriched.	[41]
SK35-27	−17°	00.400'	56°	01.500'	4528			
SK35-26	−16°	00.000'	55°	59.500'	4130			
Rio Grande Rise								
RGR	-	-	-	-	-	Hydrogenetic	-	(This paper)

2. Materials and Methods

2.1. Samples

This work is based on four sets of Fe–Mn nodule samples representative of different genetic conditions (Table 1); (1) Four mixed-type Fe–Mn nodules from the CCZ in the Pacific Ocean were collected during cruise JC120 aboard the RRV James Cook (Table 1); (2) Five mixed-type nodules from the CIB were collected during cruises of RV Akademik Alexander Sidorenko, R.V. Farnella, and RV Skandi Surveyor; (3) Three hydrogenetic nodules from the MB in the Indian Ocean were collected during cruise SK35 on the ORV Sagar Kanya (Ministry of Earth Sciences (MoES)), Delhi, India); and (4) one hydrogenetic Fe–Mn coated pebble from Rio Grande Rise (RGR) in the southwest Atlantic was collected during cruise Iatá-Piuna aboard the RV Yokosuka.

The bulk chemical composition of nodules from the CCZ is uniform across the whole region according to analyses of more than 300 nodules, all pointing to a mixed-type genesis, with variable influence of hydrogenetic and diagenetic precipitation [25,39]. Bulk analysis of nodules from the CIB show a predominant hydrogenetic origin with variable proportions of diagenetic input [22]. Bulk analysis of nodules from the MB on small, spheroidal, Fe–Co–REE-rich nodules with a smooth surface show typical characteristics of hydrogenetic nodules [21,41]. Fe–Mn deposits from the RGR have not been studied so far, however recent scientific expeditions to the RGR have found ferromanganese crust, evincing that hydrogenetic precipitation occurs in the area. This is the first study showing geochemical and morphological data for that region.

The nodules were photographed, sized, and scanned using CT. Next, thin sections with approximately 100 μm thickness were prepared from nodules JC120-104B, AAS21-DR19, SS4-280G, SK35/24B, and SK35/26A to be used for SEM-EDS and μXRF . The thin sections were prepared by impregnating a slice of nodule with a mixture of Epoxiglass 1204 resin, Epoxiglass 1604 hardener, and alcohol to promote the mixture penetration, followed by heating on a hot plate at 50 $^{\circ}\text{C}$ to evaporate the alcohol, and then cutting, grinding, and polishing the slice to 100 μm .

2.2. Computed Tomography

Three-dimensional CT scans were run using Versa XRM-510 Xradia equipment from Zeiss at the Technological Characterization Laboratory from Escola Politécnica, University of Sao Paulo. Each nodule was scanned for 2 h while turning under a 160 kV 10 W X-ray source. Voxel size was 55 μm and detector resolution was 1024 \times 1024 pixels, with a transmission of 8% to 19%. The movies are available in Supplemental Data.

2.3. SEM-EDS

SEM was performed using a Leo 440i from Leo Electron Microscopy Ltd (São Paulo, Brazil) at the Laboratory of Scanning Electron Microscopy (LabMEV), Instituto de Geociências, Universidade de São Paulo, São Paulo, Brazil. Analyses were performed at high vacuum condition with Electron High Tension (EHT) of 20 keV, Work Distance (WD) of 25 mm and Iprobe of 1.0–2.0 nA (probe current). EDS was performed using a Si (Li) solid state detector with INCA 300 software from Oxford Microanalysis group. Both Backscatter Electron (BSE) and Secondary Electron (SE) modes were acquired but only the BSE mode data are used in the results section.

2.4. Micro-X-ray Fluorescence ($\mu\text{-XRF}$)

Synchrotron radiation analyses applied in this work included $\mu\text{-XRF}$ performed at the Brazilian Synchrotron Light Laboratory (LNLS, Campinas, Brazil), Beamline XRF. μXRF measurements were acquired at 10 keV in triplicate at selected points in order to obtain element composition. Next, 0.1 mm wide transects across the nodules were performed at steps of 0.02 mm and count time per point of 600 ms, with a velocity of 0.0328 mms^{-1} to get maps of element distribution. Filters of Fe 3 μm plus Fe 6 μm were used because of the high content of Fe in the samples, which caused dead time of

nearly 100%. After adding the filters, the dead time dropped to less than 10%. The spectra were then processed using the open software PyMCA Software Version 5.1.2, downloaded from the PyMCA website [42], where the curves were calibrated, Excel files generated, and color maps obtained.

3. Results

3.1. Morphology of Nodules

Nodules from the CCZ have an average length of 8 cm. The shape is discoidal and some nodules may exhibit a pronounced rim marking the transition between a botryoidal top-surface texture and a rough bottom-surface texture (Figure 1 JC120-104A to JC120-104D), reflecting their mixed-type genesis. The rim corresponds to the boundary between the buried and the exposed portion of the nodules. The mixed-type nodules from the CIB are 3–6 cm long (Figure 1 AAS21-19 to F8-398A), with spheroidal to elongate shape, except for nodule F8-398A that is faceted. These nodules have a rough to smooth surface with no obvious pattern. Hydrogenetic nodules from the MB are 4 cm long on average, strongly spheroidal or elongate, and have a micro-botryoidal surface (Figure 1 SK35-27 to SK35-24). The coated pebble from the RGR is 2 cm long, spheroidal, with a micro-botryoidal surface (Figure 1 RGR).

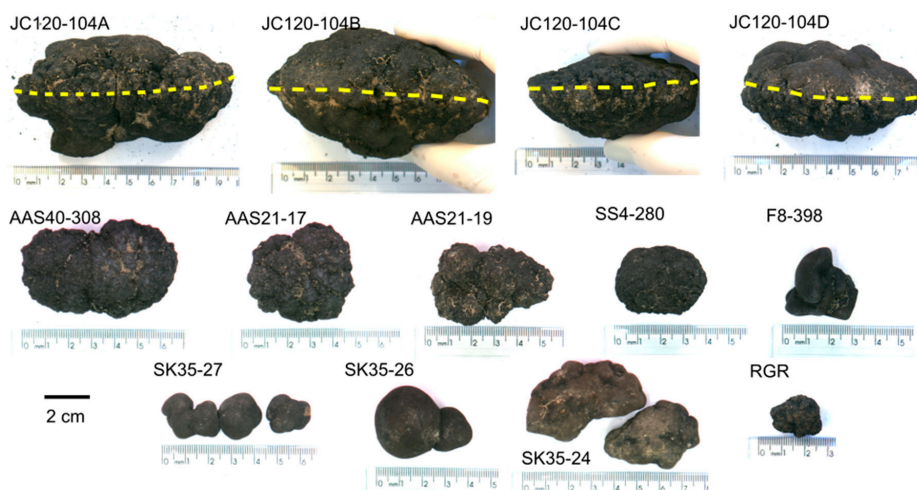


Figure 1. Mixed-type nodules from the Clarion-Clippertone Zone (JC104-120A to JC104-120D) and the Central Indian Ocean Basin (AAS21-19 to F8-398A); hydrogenetic nodules from the Mascarene Basin (SK35-27 to SK35-24) and hydrogenetic Fe–Mn oxide-coated pebble from the Rio Grande Rise (RGR). Yellow dashed lines mark the pronounced rim.

3.2. Texture and X-ray Absorbance

The computed tomography videos (Supplementary Material Videos S1–S4) reveal the internal structures of the nodules in three dimensions. In these images, bright color means high absorbance of X-rays and corresponds to denser material, while dark color means low absorbance of X-rays and corresponds to less dense materials.

The hydrogenetic nodules from MB show a bright, dense, and homogeneous Fe–Mn oxide layer, contrasting with the dark material of the nuclei (Figure 2A,B); some are poly-nodules (Figure 2A). The nuclei shape is rounded or irregular and variable in size, from 5 mm to 40 mm, and corresponds to about 10% the nodules volume in sample SK35-26 and 90% of the nodules volume in sample SK35-24 (Figure 2A,B). In both cases, the nuclei are composed by sedimentary rocks, most likely carbonates. Laminae are distinguishable at the scale of micrometers, as revealed by SEM photomicrographs (Figure 2C). The laminae are columnar, 0.2–0.5 mm thick, alternating between bright and light grey, which indicate a weak density contrast in the nodule. The columnar fabric has a minor amount of micropores, generally smaller than 50 μm . The tomography also reveals the presence of pervasive fractures in a spherical nodule (Figure 2A).

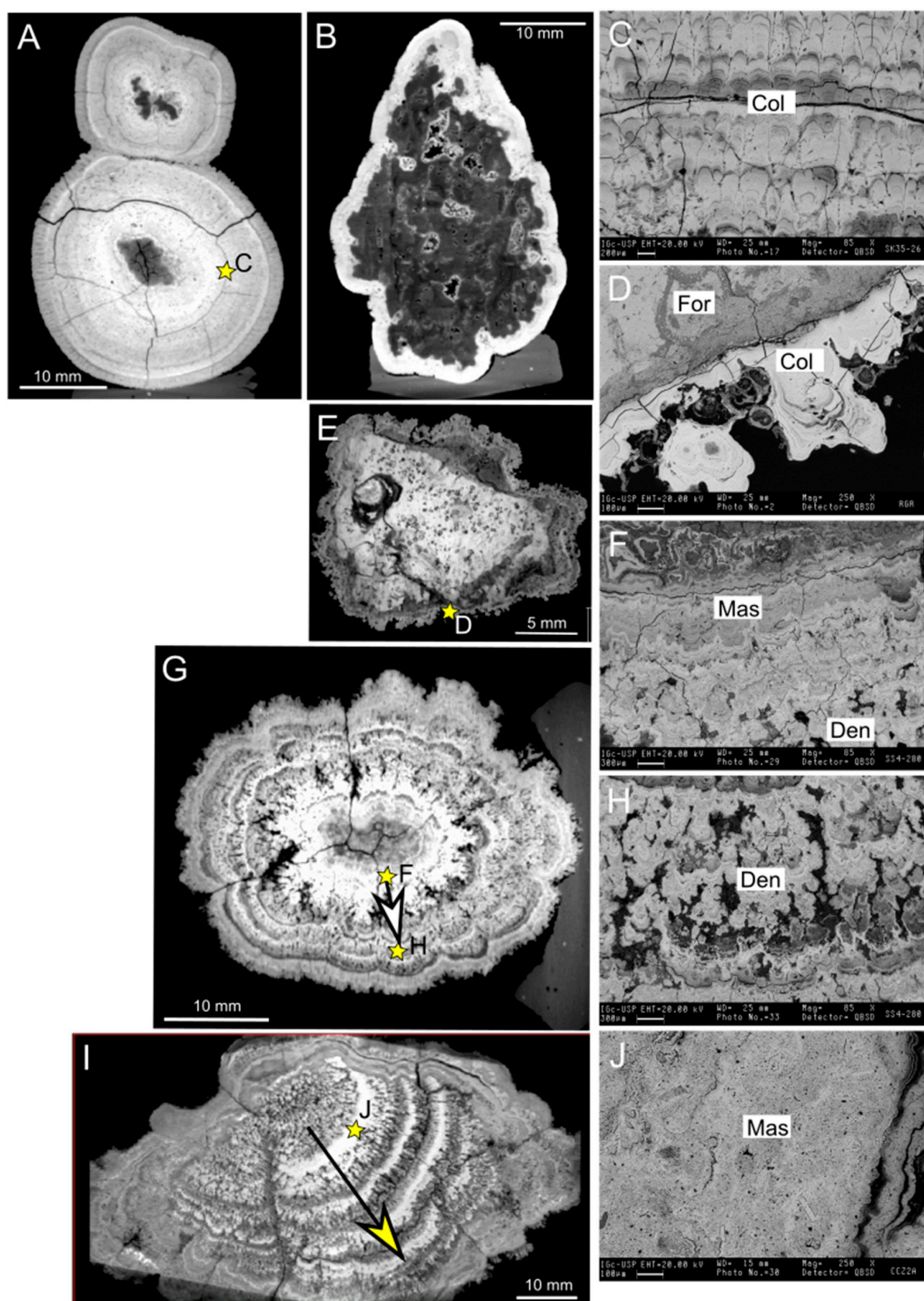


Figure 2. Internal structures of Fe–Mn nodules as revealed by Computed Tomography (left) and back-scatter Scanning Electron Microscopy (right). (A,B) Hydrogenetic Fe–Mn nodules SK35-26 and SK35-24 from the Mascarene Basin; (C) columnar texture of sample SK35-26; (D) layer of hydrogenetic Fe–Mn coating of sample RGR from Rio Grande Rise; (E) hydrogenetic Fe–Mn coated pebble RGR from the Rio Grande Rise; (G) mixed-type nodule SS4-280 from the Central Indian Basin, white arrow indicates the transition between massive and dendritic textures detailed in images (F) to (H); (I) mixed-type nodule JC120-104B from the Clarion-Clippertone Zone, in which the yellow arrow shows the growth direction; (F) massive texture in nodule SS4-280; (H) dendritic texture in nodule SS4-280; and (J) massive texture in nodule JC120-104D. For = foraminifer test, Col = columnar, Den = dendritic and Mas = massive.

The tomography of the coated pebble from RGR shows a bright, thin oxide layer formed around a relatively large nucleus of 1.8 cm long and faceted in shape, which accounts for more than 90% of the sample volume (Figure 2E). Because of this, it can be best classified as a coated pebble instead of a Fe–Mn nodule. The pebble is composed of limestone (cemented carbonate ooze) in which foraminifer tests are seen (Figure 2D). The Fe–Mn coating is composed of a single laminated to columnar oxide layer 0.5 to 0.3 mm thick (Figure 2D) and may represent the first stage of a growing nodule.

The internal structure of the mixed-type nodules differs markedly from the hydrogenetic ones. The former have 1–3 mm thick laminae with a strong density contrast (Figure 2G,I), indicating a difference in composition. The tomography reveals two types of laminae: bright, dense, massive laminae alternating with gray and porous laminae. SEM photomicrographs confirm that the bright laminae of high absorbance are massive, with no growth structures (Figure 2J). On the other hand, the gray laminae of low absorbance show a dendritic fabric, where precipitation occurred at points of preferred growth and converged afterwards, leaving behind abundant pore spaces, as large as 1.5 mm (Figure 2H). The transition between a massive-dendritic texture to a dendritic one is seen in Figure 2F–H.

Nodules from the CCZ show a contrast between the nucleus and adjacent laminae, and structural differences between the inner (older) and outer (younger) layers (Figure 2G). The older layers show alternation between 1–3-mm thick porous dendritic laminae with massive laminae. This portion of the nodule apparently grew in a preferred direction, resulting in a conical geometry indicated by the yellow arrow in Figure 2G. The younger layers, in contrast, alternate between thin (50–200 μm) bright laminae and gray laminae that wrap around the internal portion of the nodule, which most likely served as a nucleus for the external portion. This way, the nuclei of the samples from the CCZ are composed by fragments of older manganese nodules that are rounded in shape and 5 cm long on average, which correspond to about 70% of the nodules volume (Figure 2I).

Nuclei of nodules from the CIB are rounded, 3–8 mm long, and correspond to up to 30% of the nodules volume (Figure 2G). They are most likely composed of sedimentary rocks.

3.3. Chemical Composition across the Nodules

SEM-EDS element mapping of the outer margin part of mixed-type CCZ nodule JC120-104D (Figure 3) shows a clear anti-correlation between porous Mn-rich laminae (green) and massive Fe-rich laminae (blue). Mn-rich laminae show higher abundance of Ni (orange), while Fe-rich laminae show higher abundance of Ti (gray). High Si content occurs within the pore spaces where detrital material is more likely to be present.

Similarly, μ -XRF element distributions reveal a distinct alternation between Mn-rich and Fe-rich laminae in mixed-type nodules (Figure 4, samples JC120-104B, AAS21-19, SS4-280). This Mn versus Fe alternation is not observed in hydrogenetic nodules (Figure 4, samples SK35-26, SK35-24) or in the coated pebble from RGR (Figure 4, sample RGR). Nevertheless, Mn/Fe ratios from 1 to 40 show that Fe is not completely absent in Mn-rich laminae and vice versa.

A mixed-type nodule from the CCZ (sample JC120-104B) exhibits Mn/Fe ratios varying between two and 40 with a mean value of 10. The highest Mn/Fe ratios (up to 40) are found in the massive laminae in the older parts of the nodule. Both mixed-type nodules from the CIB (samples AAS21-19 and SS4-280) show Mn/Fe ratios between 0.5 and 10, with the lowest value in the Fe–Mn oxide layer closest to the nuclei. On the other hand, the hydrogenetic nodules (samples: SK35-26 and SK35-24) show clear differences from the mixed-type nodules because they exhibit Mn/Fe ratios close to 1 through most of the growth laminae. The coated pebble from RGR shows Mn/Fe ratios of <1 .

Element distribution maps of Cu, Ni, and Co reveal that Ni and Cu follow the distribution of Mn, while Co follows the distribution of Fe in the mixed-type nodules (Figure 4, samples JC120-104B, AAS21-19, SS4-280). In the maps, Cu is indicated in red and Ni in blue, which results in a purple color where both elements are present. Therefore, fractionation occurred between Cu + Ni and Co in these nodules. In contrast, the hydrogenetic nodules (Figure 4, samples SK35-24, SK35-26) and the coated

pebble from RGR differ from the mixed-type nodules in that they are significantly and homogeneously enriched in Co, instead of Cu and Ni.

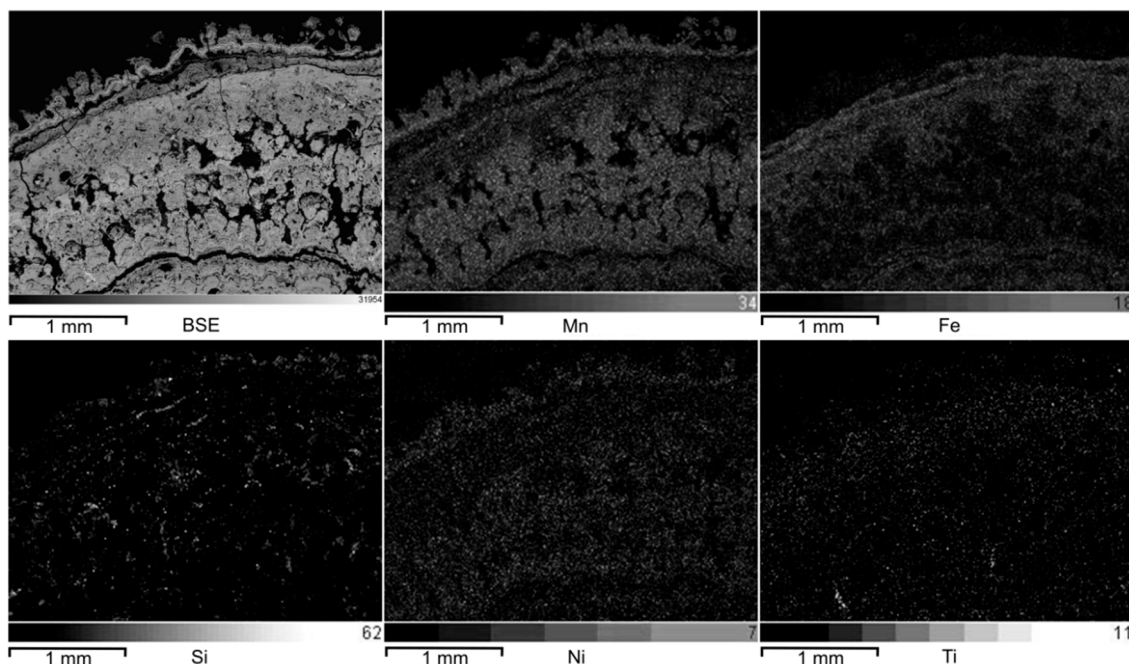


Figure 3. SEM backscatter electron photomicrograph and EDS element distribution maps for Mn, Fe, Si, Ni and Ti at the outer rim of the mixed-type nodule JC120-104B from the Clarion-Clipperton Zone.

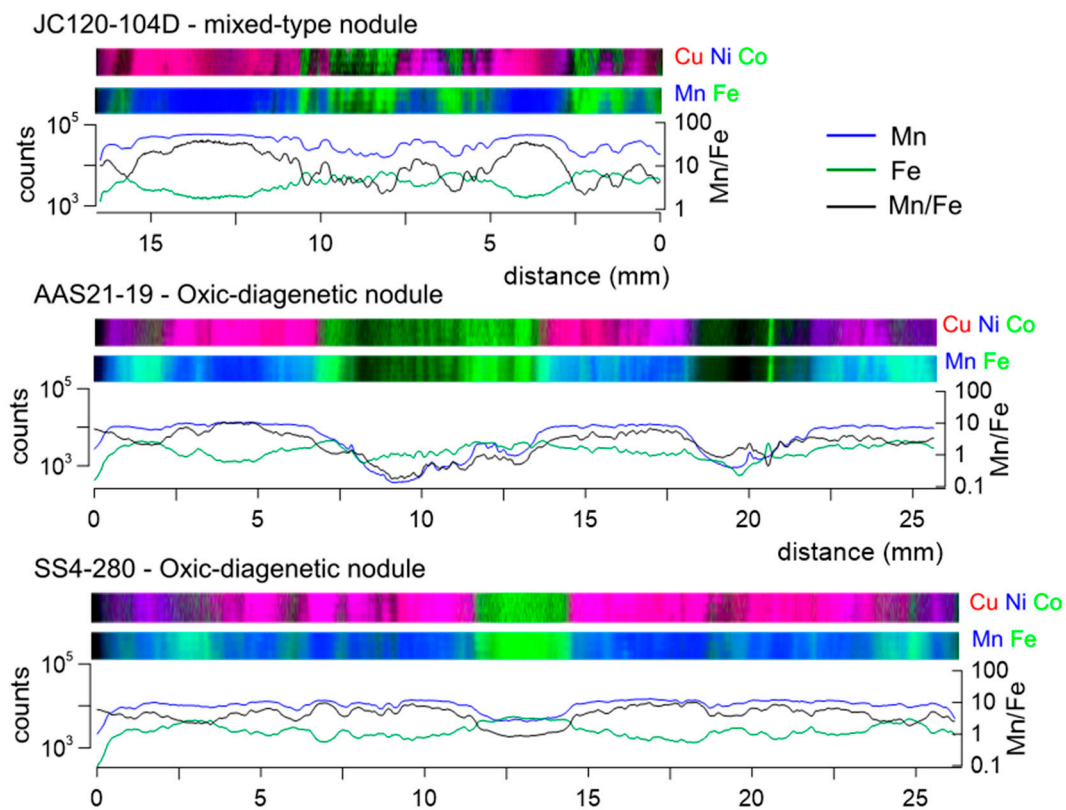


Figure 4. Cont.

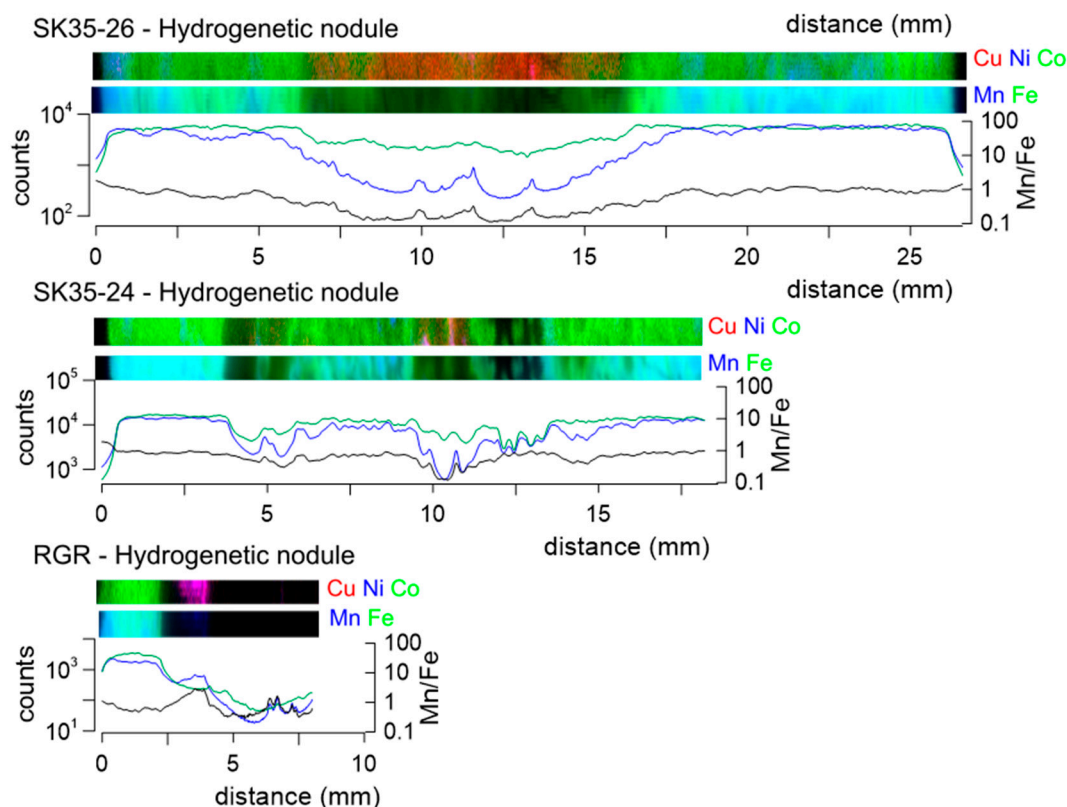


Figure 4. μ -XRF mapping of Mn, Fe, Cu, Ni, and Co distributions and Mn, Fe and Mn/Fe ratio curves along a transect across mixed-type nodules (JC120-104B, AAS21-19 and SS4-280), hydrogenetic nodules (SK35-26 and SK35-24), and hydrogenetic Fe–Mn coated pebble from Rio Grande Rise (RGR). Purple color corresponds to the mutual presence of the elements indicated by red (Cu) and blue (Ni), and light blue corresponds to the mutual presence of the elements indicated by blue (Mn) and green (Fe).

4. Discussion

4.1. Geochemistry, Texture, and X-ray Absorbance of Laminae

The geochemical and morphological characterization presented here for the nodules from the CCZ, CIB, MB, and RGR allows for a rigorous and integrated characterization of Fe–Mn nodules that provides another dimension to previously established classification methods.

Data from CT and SEM-EDS suggest homogeneity for hydrogenetic nodules and a complex heterogeneity for the mixed-type nodules. X-Ray absorbance, for both CT and SEM data, seems to result from the amount of pore space (i.e., material density) instead of the chemical composition (i.e., atomic mass) of the laminae. This explains why both massive Mn-rich laminae from the mixed-type nodules and columnar laminae from the hydrogenetic nodules present high absorbance.

The bright, dense, and columnar laminae of the hydrogenetic nodules are associated with a relatively homogeneous chemical composition, with Fe and Mn present in the same amount and with no variations in trace element contents, all pointing to a single source of metals. The same result is also observed for the hydrogenetic Fe–Mn coated pebbled from RGR, which is an example of a purely hydrogenetic Fe–Mn oxide, precipitated in an oxic environment. This is in line with previous work showing that hydrogenetic nodules form on a firm sediment substrate such as red clays or within unconsolidated oxic sediment. Under these conditions, pore water has a chemical composition equal to that of bottom seawater, which rules out significant contributions of diagenetic reduced Mn species [4,8,11,14,41]. We suggest that the supply of Mn, Fe, and trace elements from bottom seawater may have been constant during the time of formation of the hydrogenetic nodules studied here.

The characteristics of mixed-type nodules are more complex. The rough surface suggests that they may have formed partially or totally buried in the sediment [4]. Still, the internal portions of the CCZ nodules likely correspond to a former nodule that experienced environmental conditions different from the ones during which the more recent layers formed. An abrupt contact between the older and younger portions indicates that the older nodule may have undergone partial dissolution before being covered by a second episode of oxide precipitation that resulted in the formation of the younger layers.

The CIB nodules show alternation between massive to laminated Mn–Ni–Cu-rich laminae and dendritic Fe–Co-rich laminae (Figure 5). The laminated Mn–Ni–Cu-rich laminae have Mn/Fe ratios between 5 and 10, which is indicative of diagenetic precipitation [7,33,43,44], while the dendritic Fe–Co-rich laminae have Mn/Fe ratios close to 1, which suggests that these nodules experienced episodes of hydrogenesis under oxic conditions and diagenesis under suboxic conditions. Dendritic fabric has largely been associated to diagenetic precipitation because the pore space of the sediments leads to formation of isolated rosette-like structures that eventually merge together, capturing sediment particles [25]. However, every layer formed in contact with sediments is not diagenetic. The same process can occur if hydrogenetic precipitation occurs within the upper oxic sediment, leading to dendritic hydrogenetic laminae. Dendritic patterns in hydrogenetic columnar laminae were previously observed in mixed-type nodules [30].

The flux of Mn^{3+} and Mn^{4+} to diagenetic nodules is greater than their flux from ocean water to purely hydrogenetic nodules. This occurs because Mn^{3+} and Mn^{4+} are oxidized from Mn^{2+} that is supplied by anaerobic diagenesis of organic matter within the sediments. Under reducing conditions within the sediment, Mn^{2+} , as well as Ni^{2+} and Cu^{2+} , are released from Mn oxides [20]. This occurs below the suboxic-anoxic front, centimeters to meters below the sediment surface where the nodules formed. However, these divalent cations diffuse upwards and may reach the oxic sediment if the suboxic zone in which they diffuse to is near the seafloor [11,32,35]. Because Ni^{2+} and Cu^{2+} are stable in the oxic and suboxic environments, they remain in the 2+ oxidation state, while Mn^{2+} is oxidized and made available for nodule formation as Mn^{3+} and Mn^{4+} [33,45].

Similarly, the mixed-type nodules from CCZ also show alternating hydrogenetic and diagenetic laminae. Nevertheless, the latter have Mn/Fe ratios of up to 40, which have been attributed to precipitation of Mn oxides in a suboxic environment [11,24], where a higher flux of Mn^{2+} is supplied to the pore water and can therefore contribute to further nodule formation after oxidative precipitation [19]. Wegorzewski and Kuhn (2014) described the influence of suboxic diagenesis in mixed-type nodules from the same region, in which they found laminae with Mn/Fe ratios up to 800 and a massive texture alternating with laminae with low Mn/Fe ratios of 1 to 4. These authors concluded that episodes of suboxic conditions occurred during nodule formation. Here, we found the high Mn/Fe ratio is associated with several millimeters thick massive and bright laminae from tomography data.

Mixed-type nodules from the CIB have been described as those containing higher proportions of hydrogenetic phases in contrast to about 80% of diagenetic proportions in the eastern CCZ nodules [25], from where the samples used here come. The CIB sediments contain more terrigenous material [46], which dilutes the supply of organic matter to the seafloor and reduces the amount of mobilized metals from diagenesis [25].

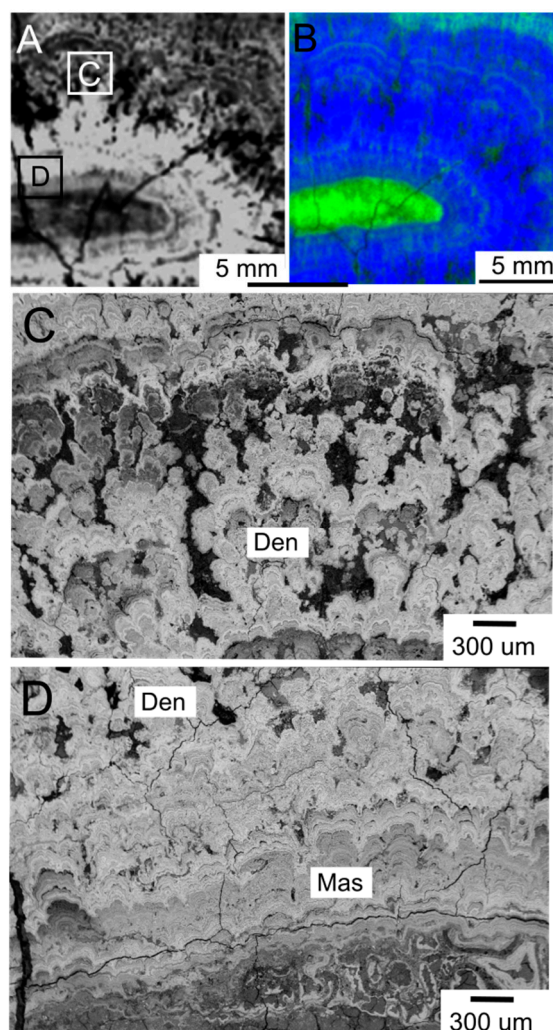


Figure 5. Mixed-type nodule SS4-280 from the Central Indian Basin. (A) Detail from computed tomography image and (B) μ -XRF mapping (blue = Mn, green = Fe, and light blue shades means presence of both). Insets in (A) show transition from (D) massive to (C) dendritic texture. SEM micrographs were obtained in BSE mode. Den = dendritic and Mas = massive.

4.2. The Role of the Oxic-Suboxic Front (OSF)

The geochemistry and internal structure of the nodules studied reflects the location of the OSF within the sediment where they formed. For the hydrogenetic nodules, the OSF is either too deep in the sediment to contribute to nodule growth, in which case the dissolved Mn^{2+} that migrated into the suboxic sediment does not reach the surface sediment oxic zone where the nodules are forming; or the OSF is absent, such as in red clay environments (Figure 6A). In mixed-type nodules, however, the OSF is of fundamental importance.

Periods of hydrogenetic precipitation within the sediment are only possible when the OSF is deep in the sediment and hence the metals coming from seawater are dominant (Figure 6B). For the eastern CCZ, the OSF has recently been measured to occur at about 2–3 m depth in the sediment within areas where mixed-type nodules occur [35], which concurs with hydrogenetic current growth laminae of the nodules form from precipitation in that area. On the other hand, diagenetic precipitation is only possible when the OSF is close to the seafloor, so that the metals can diffuse up-section to reach the nodules (Figure 6C,D). At the Peru Basin, where nodules are known to have a predominant diagenetic origin, the OSF is currently located at 10 cm below the sediment surface [47] although it may have been shallower in the past.

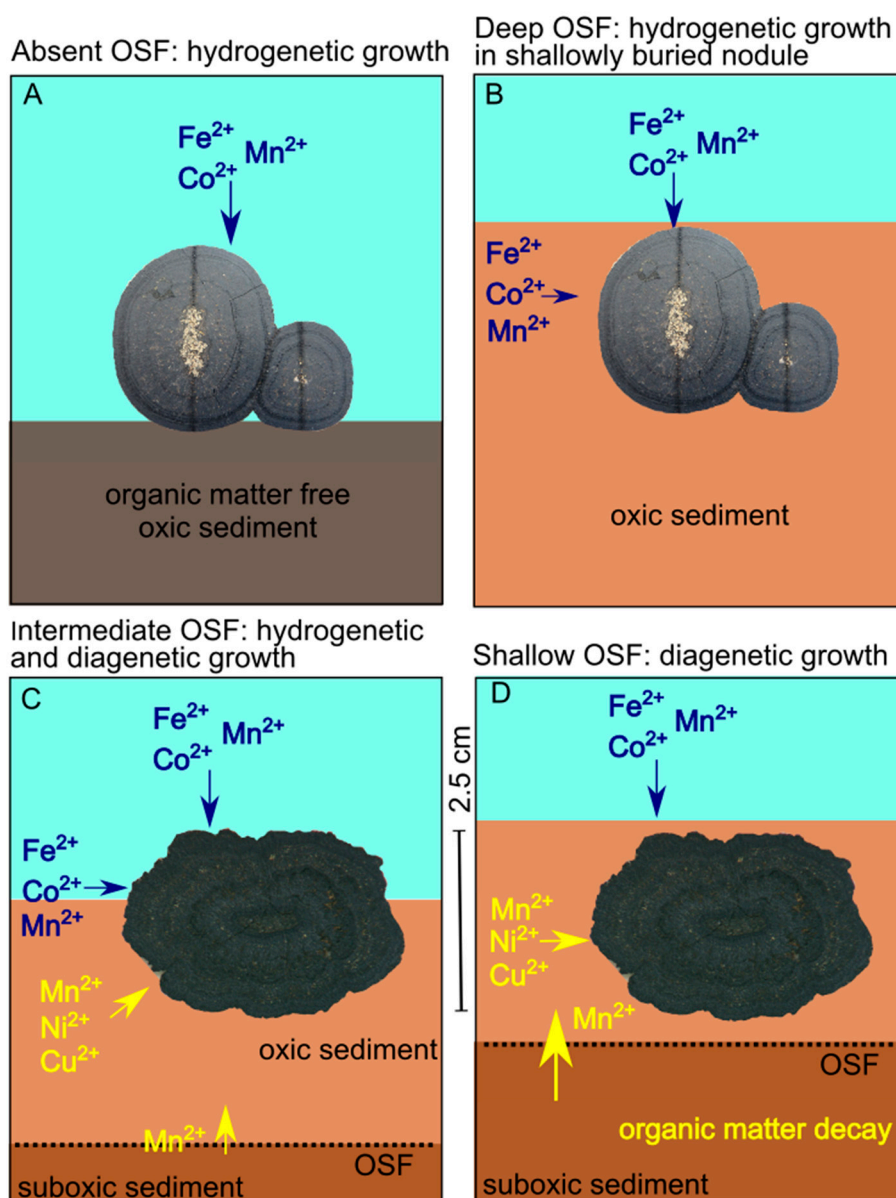


Figure 6. Schematic model suggesting the environmental conditions of formation of different genetic types of ferromanganese nodules. OSF = oxic-suboxic front. (A) Stiff sediment or organic matter-free oxic sediment where metals come from seawater only (blue); (B) Oxic sediment with a relatively deep OSF, with metals mainly sourced from seawater. (C) OSF is closer to the sea floor and the availability of metals from diagenetic reactions Mn, Ni, and Cu (yellow) increases; (D) OSF is near the base of the nodule and the main source of metals is pore water within suboxic sediment.

A third scenario occurs when the OSF is shallow enough that suboxic sediments are closer to the base of the nodules. In this case, the source of Mn^{2+} from below the OSF (lower suboxic zone) is more important to nodule formation, and Mn^{2+} will directly undergo oxidative precipitation on the nodule surface (Figure 6D). The heterogeneity within the mixed-type nodules, as well as the relative role of hydrogenetic and diagenetic process, will depend on the vertical migration of OSF, which reflects the input of organic material and therefore productivity in surface waters. Many studies attributed the OSF depth fluctuation to changes in oceanic primary productivity, which directly affect the flux of organic matter to the sediment [19,24,33,35,48].

This variability has been documented in the literature, in terms of micro-rhythmic alternation of Mn/Fe ratios and trace element content in nodules [24,49,50]. Here, we show that the micro-rhythmic

alternation can be observed also by CT tomography, SEM, and μ -XRF analyses. This alternation of Mn/Fe ratios is ultimately linked to fluctuations in the OSF depth. For example, the Mn-redox boundary fluctuated between 5 and 25 cm over the past 400 kyr in the MANOP site H (nodule field), in the eastern equatorial Pacific [51].

The mixed-type nodules from the eastern CCZ seem to be more strongly influenced by the OSF fluctuation compared to the nodules from the CIB. Since the CCZ lies just north of the surface high primary productivity zone of the equatorial Pacific Ocean, it should be impacted by fluctuations in the flux of organic matter to the seafloor. In fact, the OSF location in the sediment have been fluctuating due to long-term (glacial/interglacial) and short-term (ENSO system) oscillations of surface-water primary productivity in the Peru Basin [52], located just south of the high surface-water primary productivity zone of the equatorial Pacific Ocean. Consequently, we infer that surface-water primary productivity fluctuation occurred frequently in the CCZ.

5. Conclusions

We present new insights into the genesis of deep-ocean Fe–Mn nodules based on computed tomography, SEM-EDS, and μ -XRF analyses, demonstrating how these techniques can be used to infer fluctuations in the oxic-suboxic front that occurred during the growth history of nodules. From these analyses, we conclude that:

1. The proportion of hydrogenetic and diagenetic processes in mixed-type nodules is reflected by their geochemistry, texture, and X-ray absorbance. High-absorbance areas correspond to massive Mn-rich laminae, while low-absorbance areas correspond to dendritic Mn-depleted laminae. The ratio of these laminae types ultimately reflects changes in the location of the OSF within the sediment, which in turn reflects variations in surface-water productivity.
2. Mixed-type eastern CCZ nodules show a higher suboxic diagenetic influence than mixed-type CIB nodules;
3. The micro-rhythmic distribution of Mn, Fe, Ni, Cu, and Co in the mixed-type nodules show micrometer- to millimeter-thick laminae that are chemically and texturally heterogeneous compared to their uniform bulk chemistry. In contrast, oxic hydrogenetic nodules are compositionally homogeneous, which reflects comparable seawater and pore-water compositions;
4. Changes in oceanographic conditions such as fluctuation of surface-water primary productivity, changes in sediment accumulation-erosion rates, and fluctuation of deep-ocean ventilation are possible drivers of depth variations in the sediment of the OSF, which controls the availability of Mn, Ni, and Cu to nodule growth. This process ultimately results in micro-rhythmic alternation in chemical composition and textures in mixed-type nodules.
5. Fluctuations of surface-water primary productivity probably occurred more frequently in the CCZ compared to the CIB, driving the formation of massive up to 3-mm thick, strongly Mn-enriched laminae (Mn/Fe up to 40) in the CCZ nodules; whereas detrital accumulation rates were higher and more varied as reflected in CIB nodule laminae.

Supplementary Materials: The following are available online at <https://zenodo.org/record/1471960#.W9LcfVLFKJ0>, Video S1: Three-dimensional computed tomography of sample JC120-104B; Video S2: Three-dimensional computed tomography of sample SS4-280; Video S3: Three-dimensional computed tomography of sample SK35-26; Video S4: Three-dimensional computed tomography of sample RGR.

Author Contributions: Conceptualization, J.H.; Data curation, M.B.; Analyses, M.B.; Funding acquisition, B.M. and L.J.; Methodology, D.G.; Project administration, L.J.; Resources, B.N.N. and B.M.; Software, D.G.; Supervision, C.M. and L.J.; Writing original draft, M.B.; Writing, review, and editing, M.B., C.M., J.H., B.N.N., B.M. and L.J.

Funding: This research was funded by FAPESP, grant number 2014/50820-7. M.B. was granted with scholarship by the Coordenação de Aperfeiçoamento de Pessoal de Nível Superior—Brasil (CAPES)—Finance Code 001. The samples from the CCZ were acquired during the MIDAS project, funded under European Union Grant Agreement n° 603418. The CIB and MN nodules were collected during the cruises funded by Ministry of Earth Sciences, Government of India.

Acknowledgments: We thank Paulo Sumida (Benthic Dynamics Laboratory, IO-USP), for the donation of the sample from the Rio Grande Rise. We also thank the Brazilian Synchrotron Light Laboratory by providing facilities for the measures with synchrotron light, special thanks for Carlos Perez for assisting us with the experiments. B.N.N. would like to appreciate the services of B. Vijaykumar for the efficient Minerals 2018, 8, 488 14 of 16 upkeep of manganese nodule repository at NIO.

Conflicts of Interest: The authors declare no conflict of interest.

References

1. Cronan, D.S. Deep-sea nodules: Distribution and geochemistry. In *Marine Manganese Deposits*; Glasby, G.P., Ed.; Elsevier: Amsterdam, The Netherlands, 1977; pp. 11–44.
2. Glasby, G.P. *Marine Manganese Deposits*; Glasby, G.P., Ed.; Elsevier: Amsterdam, The Netherlands, 1977; pp. 1–524.
3. Mero, J.L. *The Mineral Resources of the Sea*; Elsevier: Amsterdam, The Netherlands, 1965; pp. 1–312, ISBN 0444403949.
4. Halbach, P.; Scherhag, C.; Hebisch, U.; Marchig, V. Geochemical and mineralogical control of different genetic types of deep-sea nodules from the Pacific Ocean. *Miner. Depos.* **1981**, *16*, 59–84. [[CrossRef](#)]
5. Hein, J.R.; Petersen, S. The geology of manganese nodules. In *Deep Sea Minerals: A physical, Biological, Environmental, and Technical Review*; Baker, E., Beaudoin, Y., Eds.; Secretariat of the Pacific Community: Noumea, New Caledonia, 2013; pp. 7–18, ISBN 978-82-7701-119-6.
6. Halbach, P.; Friedrich, G.; Von Stackelberg, U. *The Manganese Nodule Belt of the Pacific Ocean: Geological Environment, Nodule Formation and Mining Aspects*; Halbach, P., Friedrich, G., Von Stackelberg, U., Eds.; Ferdinand Enke: Stuttgart, Germany, 1988; pp. 1–254, ISBN 3432963815.
7. Pattan, J.N.; Parthiban, G. Geochemistry of ferromanganese nodule-sediment pairs from Central Indian Ocean Basin. *J. Asian Earth Sci.* **2011**, *40*, 569–580. [[CrossRef](#)]
8. Bau, M.; Schmidt, K.; Koschinsky, A.; Hein, J.; Kuhn, T.; Usui, A. Discriminating between different genetic types of marine ferro-manganese crusts and nodules based on rare earth elements and yttrium. *Chem. Geol.* **2014**, *381*, 1–9. [[CrossRef](#)]
9. Hein, J.R.; Koschinsky, A. Deep-ocean ferromanganese crusts and nodules. In *Treatise on Geochemistry*; Scott, S., Ed.; Elsevier: Amsterdam, The Netherlands, 2014; pp. 273–291, ISBN 9780080983004.
10. Nath, B.N.; Roelandts, I.; Sudhakar, M.; Plugger, W.L.; Balaram, V. Cerium anomaly variations in ferromanganese nodules and crusts from the Indian Ocean. *Mar. Geol.* **1994**, *120*, 385–400. [[CrossRef](#)]
11. Glasby, G.P. Manganese: Predominant role of nodules and crusts. *Mar. Geochem.* **2006**, 371–427. [[CrossRef](#)]
12. Cronan, D.S.; Hodkinson, R.A.; Mineral, M.; Programme, R. An evaluation of manganese nodules and cobalt-rich crusts in south pacific exclusive economic zones. Part III. Nodules and crusts in the EEZ of Tuvalu (Ellice Islands). *Mar. Geores. Geotechnol.* **2008**, *11*, 153–174. [[CrossRef](#)]
13. Glasby, G.P. Deep seabed mining: Past failures and future prospects. *Mar. Geores. Geotechnol.* **2002**, *20*, 161–176. [[CrossRef](#)]
14. Hein, J.R.; Spinardi, F.; Okamoto, N.; Mizell, K. Critical metals in manganese nodules from the Cook Islands EEZ, abundances and distributions. *Ore Geol. Rev.* **2015**, *68*, 97–116. [[CrossRef](#)]
15. Hein, J.R.; Mizell, K.; Koschinsky, A.; Conrad, T.A. Deep-ocean mineral deposits as a source of critical metals for high- and green-technology applications: Comparison with land-based resources. *Ore Geol. Rev.* **2013**, *51*, 1–14. [[CrossRef](#)]
16. Murton, B. Seafloor mining: the future or just another pipe dream? *Underw. Technol.* **2013**, *31*, 53–54. [[CrossRef](#)]
17. Murton, B.J. A global review of non-living resources on the extended continental shelf. *Braz. J. Geophys.* **2001**, *18*, 281–306. [[CrossRef](#)]
18. Randhawa, N.S.; Hait, J.; Jana, R.K. A brief overview on manganese nodules processing signifying the detail in the Indian context highlighting the international scenario. *Hydrometallurgy* **2015**, *165*, 166–181. [[CrossRef](#)]
19. Dymond, J.; Lyle, M.; Finney, B.; Piper, D.Z.; Murphy, K.; Conard, R.; Pisias, N. Ferromanganese nodules from MANOP Sites H, S, and R-Control of mineralogical and chemical composition by multiple accretionary processes. *Geochim. Cosmochim. Acta* **1984**, *48*, 931–949. [[CrossRef](#)]

20. Lyle, M.; Heath, G.R.; Robbins, J.M. Transport and release of transition elements during early diagenesis: Sequential leaching of sediments from MANOP Sites M and H. Part I. pH 5 acetic acid leach. *Geochim. Cosmochim. Acta* **1984**, *45*, 1705–1715. [[CrossRef](#)]
21. Nath, B.N.; Roelandts, I.; Sudhakar, M.; Plugger, W.L. Rare earth element geochemistry of ferromanganese deposits from the Indian Ocean. *Geophys. Res. Lett.* **1992**, *38*, 185–208. [[CrossRef](#)]
22. Pattan, J.N.; Parthiban, G.; Amonkar, A.; Shaikh, S.A.; Jai Sankar, S. Trace elements in ferromanganese nodules from the central Indian Ocean basin. *Mar. Geores. Geotechnol.* **2017**. [[CrossRef](#)]
23. Takematsu, N.; Sato, Y.; Okabe, S. Factors controlling the chemical composition of marine manganese nodules and crusts: A review and synthesis. *Mar. Chem.* **1989**, *26*, 41–56. [[CrossRef](#)]
24. Wegorzewski, A.V.; Kuhn, T. The influence of suboxic diagenesis on the formation of manganese nodules in the Clarion Clipperton nodule belt of the Pacific Ocean. *Mar. Geol.* **2014**, *357*, 123–138. [[CrossRef](#)]
25. Kuhn, T.; Wegorzewski, A.; Rühlemann, C.; Vink, A. Composition, formation, and occurrence of polymetallic nodules. In *Deep-Sea Mining*; Sharma, R., Ed.; Springer International Publishing: Basel, Switzerland, 2017; pp. 23–63, ISBN 9783319525570.
26. Bonatti, E.; Kraemer, T.; Rydell, H. Classification and genesis of submarine iron-manganese deposits. In *Ferromanganese Deposits on the Ocean Floor*; Horn, D.R., Ed.; NSF: Alexandria, VA, USA, 1972; pp. 149–166.
27. Josso, P.; Pelleter, E.; Pourret, O.; Fouquet, Y.; Etoubleau, J.; Cheron, S.; Bollinger, C. A new discrimination scheme for oceanic ferromanganese deposits using high field strength and rare earth elements. *Ore Geol. Rev.* **2017**, *87*, 3–15. [[CrossRef](#)]
28. González, F.J.; Somoza, L.; Hein, J.R.; Medialdea, T.; León, R.; Urgorri, V.; Reyes, J.; Martín-Rubí, J.A. Phosphorites, Co-rich Mn nodules, and Fe–Mn crusts from Galicia Bank, NE Atlantic: Reflections of Cenozoic tectonics and paleoceanography. *Geochem. Geophys. Geosyst.* **2016**, *17*, 346–374. [[CrossRef](#)]
29. Mayumy Amparo, C.-R.; Arturo, C.; Marlene, O.; Rez Mayumy Amparo, C.; Arturo, C.; Marlene, O. Morphology and texture of polymetallic nodules and their association with sediments of the Mexican Pacific. *Mar. Georesour. Geotechnol.* **2013**, *31*, 154–175. [[CrossRef](#)]
30. Sarkar, C.; Iyer, S.D.; Hazra, S. Inter-relationship between nuclei and gross characteristics of manganese nodules, Central Indian Ocean Basin. *Mar. Georesour. Geotechnol.* **2008**, *26*, 259–289. [[CrossRef](#)]
31. Vineesh, T.; Nagender Nath, B.; Banerjee, R.; Jaisankar, S.; Lekshmi, V. Manganese nodule morphology as indicators for oceanic processes in the Central Indian Basin. *Int. Geol. Rev.* **2009**, *51*, 27–44. [[CrossRef](#)]
32. Cronan, D.S.; Tooms, J.S. The geochemistry of manganese nodules and associated pelagic deposits from the Pacific and Indian Oceans. *Deep Sea Res. Oceanogr. Abstr.* **1969**, *16*, 335–359. [[CrossRef](#)]
33. Verlaan, P.A.; Cronan, D.S.; Morgan, C.L. A comparative analysis of compositional variations in and between marine ferromanganese nodules and crusts in the South Pacific and their environmental controls. *Prog. Oceanogr.* **2004**, *63*, 125–158. [[CrossRef](#)]
34. Bonatti, E.; Fisher, D.E.; Joensuu, O.; Rydell, H.S. Postdepositional mobility of some transition elements, phosphorus, uranium and thorium in deep sea sediments. *Geochim. Cosmochim. Acta* **1971**, *35*, 189–201. [[CrossRef](#)]
35. Mewes, K.; Mogollón, J.M.; Picard, A.; Rühlemann, C.; Kuhn, T.; Nothen, K.; Kasten, S. Impact of depositional and biogeochemical processes on small scale variations in nodule abundance in the Clarion-Clipperton Fracture Zone. *Deep. Res. Part I* **2014**, *91*, 125–141. [[CrossRef](#)]
36. Thomson, J.; Higgs, N.C.; Croudace, I.W.; Colley, S.; Hydes, D.J. Redox zonation of elements at an oxic/post-oxic boundary in deep-sea sediments. *Geochim. Cosmochim. Acta* **1993**, *57*, 579–595. [[CrossRef](#)]
37. Manceau, A.; Lanson, M.; Takahashi, Y. Mineralogy and crystal chemistry of Mn, Fe, Co, Ni, and Cu in a deep-sea Pacific polymetallic nodule. *Am. Mineral.* **2014**, *99*, 2068–2083. [[CrossRef](#)]
38. Guan, Y.; Sun, X.; Jiang, X.; Sa, R.; Zhou, L.; Huang, Y.; Liu, Y.; Li, X.; Lu, R.; Wang, C. The effect of Fe–Mn minerals and seawater interface and enrichment mechanism of ore-forming elements of polymetallic crusts and nodules from the South China Sea. *Acta Oceanol.* **2017**, *36*, 34–46. [[CrossRef](#)]
39. Kuhn, T.; Rühlemann, C.; Wiedicke-Hombach, M. Developing a strategy for the exploration of vast seafloor areas for prospective manganese nodule fields. In *Marine Minerals: Finding the Right Balance of Sustainable Development and Environmental Protection*; Zhou, H., Morgan, C.L., Eds.; The Underwater Mining Institute: Shanghai, China, 2012; pp. 1–9.

40. Ruhlemann, C.; Kuhn, T.; Wiedicke, M.; Kasten, S.; Mewes, K.; Picard, A. Current status of manganese nodule exploration in the German license area. In *Isope Ocean Mining Symposium*; International Society of Offshore and Polar Engineers: Maui, HI, USA, 2011; pp. 168–179.
41. Nath, B.N.; Prasad, M.S. Manganese nodules in the Exclusive Economic Zone of Mauritius. *Mar. Min.* **1991**, *10*, 303–355.
42. PyMca. Available online: <http://pymca.sourceforge.net/download.html> (accessed on 22 October 2018).
43. Reyss, J.L.; Marchig, V.; Ku, T.L. Rapid growth of a deep-sea manganese nodule. *Nature* **1982**, *295*, 401–403. [[CrossRef](#)]
44. Von Stackelberg, U.; Beiersdorf, H. The formation of manganese nodules between the Clarion and Clipperton fracture zones southeast of Hawaii. *Mar. Geol.* **1991**, *98*, 411–423. [[CrossRef](#)]
45. Dillard, J.G.; Crowther, D.L.; Murray, J.W. The oxidation states of cobalt and selected metals in Pacific ferromanganese nodules. *Geochim. Cosmochim. Acta* **1982**, *46*, 755–759. [[CrossRef](#)]
46. Nath, B.N.; Rao, V.P.; Becker, K.P. Geochemical evidence of terrigenous influence in deep-sea sediments up to 8° S in the Central Indian Basin. *Mar. Geol.* **1989**, *87*, 301–313. [[CrossRef](#)]
47. Von Stackelberg, U. Growth history of manganese nodules and crusts of the Peru Basin. In *Manganese Mineralization: Geochemistry and Mineralogy of Terrestrial and Marine Deposits*; Nicholson, K., Hein, J.R., Buhn, B., Dasgupta, S., Eds.; The Geological Society of London: London, UK, 1997; pp. 153–176.
48. Halbach, P.; Marchig, V.; Scherhag, C. Regional variations in Mn, Ni, Cu and Co of ferromanganese nodules from a basin in the southeast Pacific. *Mar. Geol.* **1980**, *38*, 1–9. [[CrossRef](#)]
49. Asavin, A.M.; Daryin, A.V.; Melnikov, M.E. Microrhythmic distribution of Co, Mn, Ni, and La Contents in Cobalt Rich Ferromanganese Crusts from the Magellan Seamounts. *Geochem. Int.* **2015**, *53*, 19–38. [[CrossRef](#)]
50. Shiraishi, F.; Mitsunobu, S.; Suzuki, K.; Hoshino, T. Dense microbial community on a ferromanganese nodule from the ultra-oligotrophic South Pacific Gyre: Implications for biogeochemical cycles. *Earth Planet. Sci. Lett.* **2016**, *447*, 10–20. [[CrossRef](#)]
51. Finney, B.P.; Lyle, M.W.; Heath, G.R. Sedimentation at MANOP site H (Eastern Equatorial Pacific) over the past 400,000 years: Climatically induced redox variations and their effects on transition metal cycling. *Paleoceanography* **1988**, *3*, 169–189. [[CrossRef](#)]
52. König, I.; Haeckel, M.; Lougear, A.; Suess, E.; Trautwein, A.X. A geochemical model of the Peru Basin deep-sea floor—And the response of the system to technical impacts. *Deep. Res. Part II* **2001**, *48*, 3737–3756. [[CrossRef](#)]



© 2018 by the authors. Licensee MDPI, Basel, Switzerland. This article is an open access article distributed under the terms and conditions of the Creative Commons Attribution (CC BY) license (<http://creativecommons.org/licenses/by/4.0/>).